Giant, 19, 2024, 100315

Full-length article

Patterning of 2D second harmonic generation active arrays in ferroelectric nematic fluids

M. Lovšin [a,b,*], A. Petelin [b], B. Berteloot [c], N. Osterman [a,b], S. Aya [d,e], M. Huang [d,e], I. Drevenšek-Olenik [a,b], R.J. Mandle [f,g], K. Neyts [c,h], A. Mertelj [a], N. Sebastian [a,*]

[a] Jožef Stefan Institute, Ljubljana, Slovenia
[b] University of Ljubljana, Faculty of Mathematics and Physics, Ljubljana, Slovenia
[c] Liquid Crystals and Photonics Group, ELIS Department, Ghent University, Ghent, Belgium
[d] South China Advanced Institute for Soft Matter Science and Technology (AISMST), School of Emergent Soft Matter, South China University of Technology, Guangzhou, China
[e] Guangdong Provincial Key Laboratory of Functional and Intelligent Hybrid Materials and Devices, South China University of Technology, Guangzhou, China
[f] School of Physics and Astronomy, University of Leeds, Leeds, UK
[g] School of Chemistry, University of Leeds, Leeds, UK
[h] State Key Lab of Advanced Displays and Optoelectronics Technologies, Hong Kong University of Science and Technology, Hong Kong

Keywords: Ferroelectric nematic fluid, Second harmonic generation, Photoalignment

Ferroelectric nematic liquid crystals exhibit unique non-linear optical properties, with the potential to become transformative materials for photonic applications. A promising direction relies on the fabrication of tailored polar orientational patterns via photoalignment, thus shaping the non-linear optical susceptibility through thin slabs of the ferroelectric fluid. Here, we explore the fabrication of 2D periodic SHG active arrays in ferroelectric nematic fluids, for different materials, cell thicknesses and motifs. Based on polarizing optical microscopy observations in combination with optical simulations, second harmonic generation microscopy and interferometry, the 3D structure of the motifs is revealed. Two different 2D periodic patterns are explored, showing that the balance between flexoelectric and electrostatic energy can lead to different domain structures, an effect which is rooted in the difference between the flexoelectric properties of the materials. It is shown that by combining the surface-inscribed alignment with different spontaneous degrees of twist, 2D SHG active arrays can be obtained in the micrometre scale, in which adjacent areas exhibit maximum SHG signals at opposite angles.

1 Introduction

The widespread implementation of nematic liquid crystals in optical devices results from a combination of their large optical anisotropy, fast reorientation under the application of small electric fields and the possibility of orientational control via confinement boundary conditions. The standard nematic phase is uniaxial and non-polar, i.e. centrosymmetric, and thus non-linear optical properties such as second harmonic generation (SHG) are only observed by breaking the inversion symmetry, for example by electric poling (electric field-induced SHG, i.e. EFISHG) [1–3] or by the flexoelectric effect through spatial deformations [4]. It

* Corresponding authors.
E-mail addresses: matija.lovsin@ijs.si (M. Lovšin), nerea.sebastian@ijs.si (N. Sebastian).
Received 19 April 2024; Received in revised form 12 June 2024; Accepted 24 June 2024

 https://doi.org/10.1016/j.giant.2024.100315

should be highlighted here, that in either case, SHG signals are very weak.

The discovery of a polar version of the nematic phase, in which molecules exhibit ferroelectric ordering [5–9], has been accompanied by a range of studies showing their potential for non-linear optical (NLO) devices. Large NLO coefficients have been reported [10,11] with the same order of magnitude as classical solid materials such as β-Barium borate (BBO). This enables a wide range of Second Harmonic Generation (SHG) microscopy studies, including the polar ordering and topology during nucleation of N_F droplets at the direct isotropic to ferroelectric phase transition [12,13].

The localized tunability of the SHG signal by application of small fields was demonstrated forin-plane switching liquid crystal cells [14]. More recently, FNLCs have been demonstrated to be an efficient electric-field tunable broadband source of entangled photons based on spontaneous parametric down-conversion [15]. In the case of the cholesteric N_F counterpart [16–19] (N^*_F), it has been shown that phase-matched SHG can be generated in the photonic bandgap [20,21].

The spontaneous polarization of FNLCs highly impacts their behaviour under confinement conditions, as in addition to the orientational coupling at the surfaces, polar effects are also present. In standard polyimide rubbed surfaces, it has been shown that, for materials such as RM734 and FNLC-919, polarization orients opposite to the rubbing direction [22,23]. Thus, antiparallel rubbed cells commonly used for homogeneous alignment in non-polar nematics, result in π-twisted structures across the cell thickness [24]. Interestingly, escape into twisted structures of both handedness has been reported also for unconstrained surfaces, suggesting that, to minimize electrostatic energy, the equilibrium state in thin layers is twisted [25].

We recently explored the alignment of FNLCs in patterned photoaligned cells, showing that flexoelectric coupling between splay deformation and polarization can be used to control the polarization direction [26]. From the designed periodic splay patterns, regions of alternating polarization direction were created in regions of opposite splay. Interestingly, at the edges of the patterned splay structures, where splay changed sign, the appearance of SHG inactive disclination lines separating the opposite polarization domains was described. In contrast to the non-polar high-temperature nematic phase in which the surface inscribed splay pattern was maintained across the cell thickness, it was shown that in the polar phase, the depolarization field created by bound charges $-\nabla \cdot \mathbf{P}$ caused the escape towards a uniform orientation in the middle of the cell, i.e. the "unsplay" of the structure [26].

The combination of NLO properties and the enabled possibility of designing custom polarization structures via patterned photoalignment is highly interesting for creating NLO active arrays, spatially modulating the NLO properties. In this contribution, we explore the fabrication of 2D SHG active arrays by photopatterning of pure 2D splay modulated structures and 2D splay-bend structures. For that purpose, we study such structures by combining polarizing optical microscopy, SHG microscopy and SHG interferometry experimental investigations with simulations of spectral transmission and second-harmonic generation (SHG) for thin birefringent media. Three different materials are employed: the archetypical DIO and RM734, in comparison with the 1D splay structures already reported for them [26] and FNLC-1571, a room-temperature ferroelectric nematic material.

2 Material and methods

2.1 Materials

Three different liquid crystalline materials have been employed: DIO [5], RM734 [7,27] and FNLC-1571. The latter was provided by Merck Electronics KGaA and exhibits three distinct thermotropic LC phases, with the ferroelectric nematic phase stable at room temperature: Isotropic- 88 °C – Nematic (N) - 62 °C – modulated antiferroelectric nematic - 48 °C – ferroelectric nematic phase (N_F) - 8 °C – crystal.

DIO material trans(2,3′,4′,5′-tetrafluoro-[1,1′-biphenyl]−4-yl 2,6-difluoro-4-(5-propyl-1,3-dioxan-2-yl)benzoate) has been synthesized according to the description given in reference [28]. On cooling, DIO exhibits the N_F phase in the temperature interval 68.9 °C −60 °C on which we focused our investigations. Finally, RM734 (4-((4-nitrophenoxy) carbonyl)phenyl-2,4-dimethoxybenzoate) was synthesized according to reference [27]. Investigations of RM734 were performed in the N_F phase accessible on cooling in the temperature range 132.7 °C −90 °C. Both materials have been extensively investigated [8,9,24,29,30].

2.2 Photopatterned cell preparation

Liquid crystal cells were built by assembling two glass substrates coated with indium tin oxide (ITO) and a layer of the photo-alignment material Brilliant Yellow separated by glass spacers of different μm-size diameters. The assembled thickness of the cells employed in this study was measured to be in the interval 2.8–10.1 μm. The liquid crystal orientation at the substrate surface was defined through patterned photoalignment, which provided anisotropic nonpolar in-plane alignment without pretilt. A detailed description of the photopatterning process can be found in references [26,31]. Each cell (2×2 cm^2) was illuminated in multiple areas producing an array of different photopatterned designs with dimension 1.3×0.73 mm^2. In between the patterns, the photo-alignment material was not illuminated, and thus the studied patterns are separated by regions with random planar alignment.

2.3 Polarizing optical microscopy and Berreman calculus

POM experiments were performed in either a Nikon Eclipse or an Optiphot-2 POL Nikon microscope. Images were recorded with a Canon EOS M200 camera. The sample was held in a heating stage (Instec HCS412W) together with a temperature controller (mK2000, Instec).

To calculate transmission spectra and colour rendering images we used the diffractive transfer matrix method "dtmm" open software package [32], which uses the Berreman 4×4 matrix method. A detailed description of its implementation for the calculation of transmission spectra is given in the references [14,26] and in the online manual available at GitHub [32].

For SHG computation, we developed an iterative algorithm based on the technique presented in [33], where the authors

use a modified Berreman calculus to compute the fundamental and the SHG waves assuming weak depletion of the fundamental beam. In short, we use the Berreman calculus to compute and obtain the electromagnetic field of the fundamental wave as it propagates through the sample. We calculate the gain coefficients for the SHG wave from the obtained fundamental beam at each layer of the optical stack and propagate the generated SHG wave through the stack. Compared to the technique in [33], our method works with weak and large depletion and has a more straightforward implementation. Details of the technique can be found in reference [34]. SHG simulations were performed for RM734 patterns taking into account the dispersion of the indexes of refraction $n_{2\omega} - n_{\omega}$ depicted in Fig. SI.1, determined as described in Supplementary Note I via the wedge-cell method. Nonlinear susceptibility coefficients d_{33}=5.6 pmV^{-1} and d_{31}=0.05d_{33} are considered [10].

2.4 Second Harmonic Generation Microscopy

Second Harmonic Generation microscopy (SHG-M) and interferometry (SHG-I) were performed using a custom-built sample-scanning microscope with an Erbium-doped fibre laser (C-Fibre A 780, MenloSystems, 785 nm, 95 fs pulses at a 100 MHz repetition rate) as the laser source. In order to avoid sample degradation, the average power was adjusted to 30 mW using an ND filter. A detailed description of the setup is available in reference [26]. The setup allows for the insertion of a BBO reference crystal before the sample followed by a Michelson interferometer for time compensation between the reference and the fundamental pulse. Additionally, the phase of the reference can be adjusted by fine rotation of a glass plate mounted on a motorized rotator to perform interferometric SHG imaging (SHG-I). The final SHG-M and SHG-I images are acquired with a high-performance CMOS camera (Grasshopper 3, Teledyne Flir) with a typical integration time of 250 ms, varying dimensions in pixels with a resolution of 0.285 μm/pixel. SHG-I interferograms of the areas of interest are then calculated by computing the mean intensity and the standard error of the mean intensity.

3 Results and discussion

3.1 Pattern A: splay 2D pattern in thin cells

We first explore 2D patterns as those depicted in Fig. 1, in which in x-direction anchoring in both cell surfaces is shaped as $\mathbf{n_s} = (n_x, n_y) = (\sin(\vartheta_{surf}), \cos(\vartheta_{surf}))$, $\vartheta_{surf} = \vartheta_0 \sin(2\pi x/P)$, with $\vartheta_0 = 40°$ and the period $P = 2\pi/k = 40$ µm. In the y-direction the modulation phase is shifted by π every 40 µm. Such a pattern implies a maximum splay curvature $k\vartheta_0$ of 0.1 µm^{-1} equivalent to that studied previously for 1D patterns [26]. Cells of different thicknesses (targeted d = 3, 5 and 8 µm) were prepared. At this stage, we explored the behaviour of DIO and RM734 in

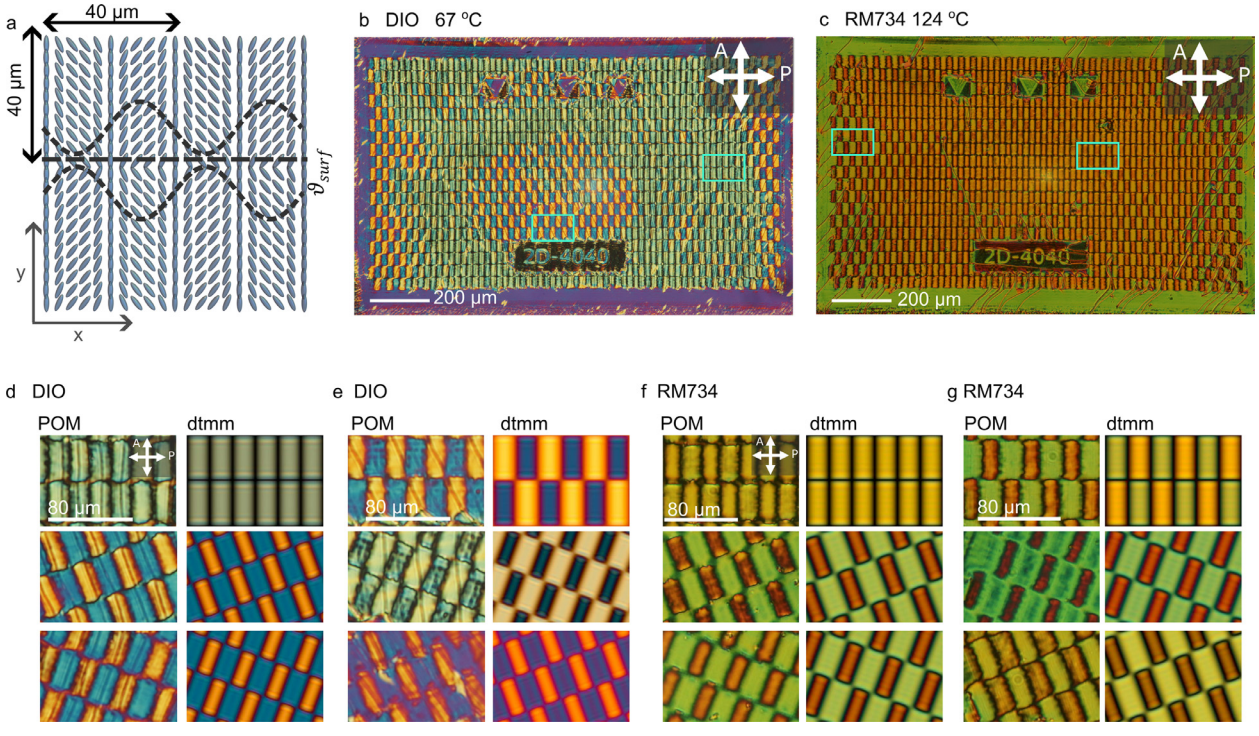

Fig. 1

2D pure splay patterns in DIO and RM734 in 3 µm cells. a) Photopatterned design inscribed in both cells' surfaces. b) POM image of the full patterned area for DIO at 67 °C under crossed polarizers. c) POM image of the full patterned area for RM734 at 124 °C under crossed polarizers. Patterns are surrounded by a frame with uniform alignment at 45° from the vertical direction. Top arrows in the pattern indicate the x-positions at which alignment corresponds with vertical direction. d,e,f&g) Zoom-in images of the blue-framed regions in b and c. POM images are compared with dtmm transmission spectra simulations in regions with monocolored and bicoloured behaviour, at extinction position and upon rotation of 20° clockwise and anticlockwise and considering structures with ξ=0.2 and ϑ_{center} 0 and 30° respectively. Double headed arrows indicate the direction of crossed polarizers. Dtmm simulations were performed considering $\Delta n = 0.19$ for DIO and $\Delta n = 0.25$ for RM734, where n_o is taken to be 1.52.

3 μm cells. The quality of the alignment was first checked in the high temperature non-polar nematic (N) phase, showing good alignment across the whole area of the design. The modulation shift across the y-direction, results in the tessellation of surface line defects at discrete y-positions as shown in Fig. SI.2.

On cooling towards the N_F phase, both materials show very different behaviour. Similarly, as reported for the 1D patterns, upon transition from the modulated antiferroelectric phase into the N_F phase, DIO initially shows the homogenization of the observed stripped texture in the intermediate antiferroelectric phase together with the appearance of defect lines parallel to the positions at which splay changes sign (lines running along y-direction) (Fig. SI.3). It should be recalled here, that in 1D patterns polarization was demonstrated to change sign across such defect lines[26]. Noteworthy, defect lines also appear at an angle in many regions of the pattern, following the diagonal of the 2D design and heavily influenced by the surrounding frame's uniform direction. Interestingly, no new defect lines are observed running along x-direction in the positions at which the phase shift occurs. Such texture remains stable for around 4° below the transition, before an additional macrostructural relaxation takes place propagating along the defect lines, characterized by the increase of the length scale of the director distortion around them. The underlying structure is preserved, as evidenced by textures (Fig. SI.3.b) . On the other hand, the texture in the direct N–N_F transition of RM734 rapidly homogenizes and although initially some faint defect lines can be distinguished (Fig. SI.4), they rapidly shrink and move out of the pattern, only remaining at a few locations near the edges of the area (Fig. SI.4).

Fig. 1.a-b shows the full patterned area for DIO (before structural relaxation) and RM734 in the N_F phase. In both cases two differentiated behaviours can be observed, showing monocolored or bicoloured optical behaviour under crossed polarizers (framed areas in Fig. 1.b-c). Qualitatively the director structure throughout the pattern and the cell thickness can be established by comparing POM observations and dtmm simulations. Let us first focus on the areas with monocolored behaviour (Fig. 1d & f), the fact that upon sample rotation, not only the intensity but also the spectral characteristics change across the pattern indicates that the prescribed alignment is not maintained in the z-direction (along the cell thickness). That is, equivalently to the simpler 1D patterns, while at the surfaces the director follows the photopatterned anchoring direction, and twists towards the cell centre in order to reduce the splay as $\vartheta(z) = \vartheta_{surf} e^{(2z^2/d^2-1/2)/\xi}$ with $\xi = 0.2$. This "unsplay" minimizes bulk bound charges due to $-\nabla \cdot \mathbf{P}$ and as inferred from POM observations, it is common for both materials. In those regions with checkerboard colour pattern at the extinction position (Fig. 1e & g), the transmitted spectra are well reproduced, considering that in addition to the described "unsplay" the director twists so as in the middle of the cell the director is at an angle ϑ_{center} of around 30° (corresponding to the diagonal direction for the half period in the x-direction and full period in the y-direction) according to:

$$\vartheta(z) = \vartheta_{surf} e^{\left(\frac{2z^2}{d^2}-\frac{1}{2}\right)/\xi} + \vartheta_{center}\left(1 - e^{\left(\frac{2z^2}{d^2}-\frac{1}{2}\right)/\xi}\right). \quad (1)$$

The final equilibrium structure is the result of a fine interplay between elastic, flexoelectric and electrostatic energies. In the present context, domain walls can be defined as a defect line/wall separating domains of differently orientated polarization. Such walls can be as simple as for example Neel's walls [28] or can consist of one or more disclination lines, as observed in DIO before the structural relaxation. If we consider the director structure deduced for DIO, where periodic defect lines appear, the "unsplay" across the cell thickness, not only reduces bulk bound charges but also reduces the surface charge associated with the polarization change at the walls with surface charge density $\sigma_P = (\boldsymbol{P}_2 - \boldsymbol{P}_1) \cdot \boldsymbol{m}$, where $\boldsymbol{P}_{1,2}$ are the polarizations of the adjacent domains and $\boldsymbol{m}$ is the normal to the wall pointing into the domain with $\boldsymbol{P}_1$ (Fig. 2a). However, by the same argument, and provided that flexoelectric coupling would be enough in this motif to promote a 2D patterning of $\boldsymbol{P}$, the structure would need to be able to equilibrate a large number of 180° strongly charged domain walls periodically in y-direction (Fig. 2a). Such walls are not observed, indicating that the energy cost of adapting to unfavourable splay is smaller than the energy cost of the strongly charged walls. This is subsequently demonstrated by SHG interferometry measurements shown in Fig. 2b & c. The interferogram for DIO shows that adjacent opposite splay signs in the x-direction have opposite directions of $\boldsymbol{P}$, while the $\boldsymbol{P}$ direction is maintained in the y-direction.

Interestingly, the fast migration outside the pattern of defect lines at the transition in the case of RM734, as opposed to the behaviour in 1D splay design (Fig. SI.5), indicates that for this material a large monodomain is obtained, where the polarization adapts to the unfavourable splay in order to prevent the larger energy cost of forming domain walls. The flexoelectric term can be included in the free energy as $\frac{1}{2}K_1|\mathbf{S} - \mathbf{S}_0|^2$ where $\mathbf{S}_0 = \gamma \mathbf{P} \cdot /K_1$, γ is the bare splay flexoelectric coefficient, K_1 is the splay elastic constant and $\mathbf{n} \cdot \mathbf{S}_0$ is the ideal splay curvature, which would minimize the splay elastic energy. It was shown that patterning through flexoelectric coupling was possible for lower splay curvatures in the case of RM734 as compared with DIO [26], indicating a smaller ideal splay curvature in the case of the former. Thus, for comparable K_1 values, the energy cost of adapting to unfavourable splay should be lower in the case of RM734 than in the case of DIO, in agreement with the observations gathered in Fig. 2. The structural difference between the areas with different in-plane angles ϑ_{center} can be attributed to the combined effect of localized asymmetries in the inscribed pattern and the minimization of electrostatic energy. Unsplaying towards an in-plane angle along the pattern diagonal causes areas of the same splay sign to connect, allowing to escape the need to adapt to unfavourable splay.

If we focus on the RM734 pattern, the recorded SHG intensity dependence on the incoming pump laser polarization shows that despite the patterned structure, the maximum intensity is obtained across the motif for incoming polarization along the y-direction, i.e. along the average director direction (Fig. 2.d-f). The effect of the patterned splay structure is only detected by the slightly larger intensity obtained in those lines in which the director is uniform across the thickness, as opposed to the regions where ϑ_{surf} deviates from y-direction. The situation differs in

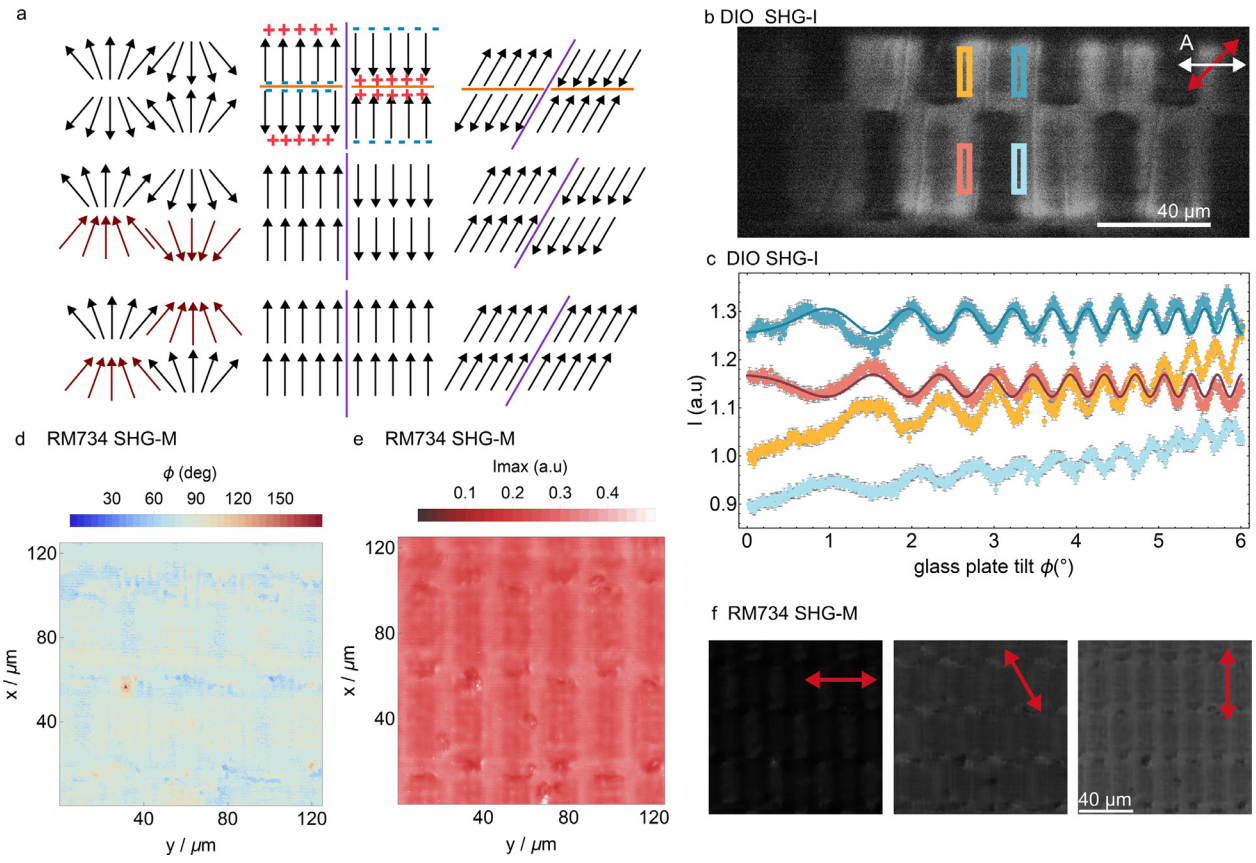

Fig. 2

Second Harmonic Generation Microscopy and Interferometry in pattern A of DIO and RM734 for thin cells, i.e. 3 µm cells. a) Schematics of the different possible weakly (purple lines) and strongly charged domain walls (orange lines), showing the orientation in the surfaces and in the middle of the cell for both, areas with $\vartheta_{center} = 0$ and $\vartheta_{center} \neq 0$. Maroon arrows indicate an unfavourable splay/polarization combination. b) SHG interferometry image and c) corresponding interferogram for the considered 2D pattern for DIO. The white arrow indicates the direction of the analyser. Data in (c) corresponds to the highlighted areas in (b), where solid lines are fits according to Supplementary Eq. 3. d&e) Analysis of the maximum SHG intensity and corresponding direction of the pump polarization of pattern A for RM734 (90° correspond to vertical direction) together with the corresponding f) SHG microscopy images, where red arrows indicate incoming pump polarization.

the case of DIO. First, the reported d_{33} value for DIO (0.24pm V^{-1}) [11] is an order of magnitude lower than that for RM734 (5.6pm V^{-1}) [10], leading to an overall lower intensity. Second, while for RM734 the d_{33} coefficient is predominant, for DIO the d_{15} coefficient also contributes notably to the signal [26]. Although the pattern exhibits a certain degree of dependence on the incoming pump polarization at which different areas have their maximum SHG signal, the overall lower signal reduces the contrast (Fig. SI.6), making them not so promising for high performance in applications.

3.2 Pattern A: splay 2D pattern in thicker cells

We additionally investigated the effect of cell thickness in the final director structure across d. For $d = 5.4$ μm cell DIO adopts the same 2D unsplay structure as can be deduced from the comparison of POM observations and dtmm simulations (Fig. S.7), and thus we will just focus on RM734. Fig. 3a & b depict the full motif as observed between crossed polarizers and with a full wave plate inserted for RM734 in 8.1 μm and 10.1 μm thick cells. In both cases, two regions spanning through a large area of the full design with different optical behaviour can be clearly distinguished, indicating the presence of twisted structures with opposite handedness. Fig. 3c & b show a zoom-in around the domain boundaries. For both thicknesses crossed-polarizers optical observations can be well reproduced considering a π-twist across d in addition to the surface inscribed pattern, i.e. $\vartheta(z) = \vartheta_{surf} \pm \pi z/d$ (Fig. 3e & f), where the difference between both regions arises from the twist handedness. It should be noted that, as shown by simulations, POM images in these twisted structures hinder obtaining information about the degree of unsplay across the thickness, as structures considering from $\xi = 10$ to $\xi = 0.2$ result in similar transmission patterns compatible with the observations (Fig. SI.8). The simulations confined in Fig. 3c & d were done considering $\xi = 1$. However, the overall twisted structure reduces electrostatic energy, compensating for the depolarization field and the increased elastic energy, as originally proposed by Khachaturyan who considered the electrostatic self-energy of $\mathbf{P}$, indicating that a ferroelectric fluid is unstable against twist perpendicular to $\mathbf{P}$ [9,35].

The SHG-M observations show that through such a combination of surface 2D splay anchoring direction and the helicoidal twist we can produce 2D SHG active patterned

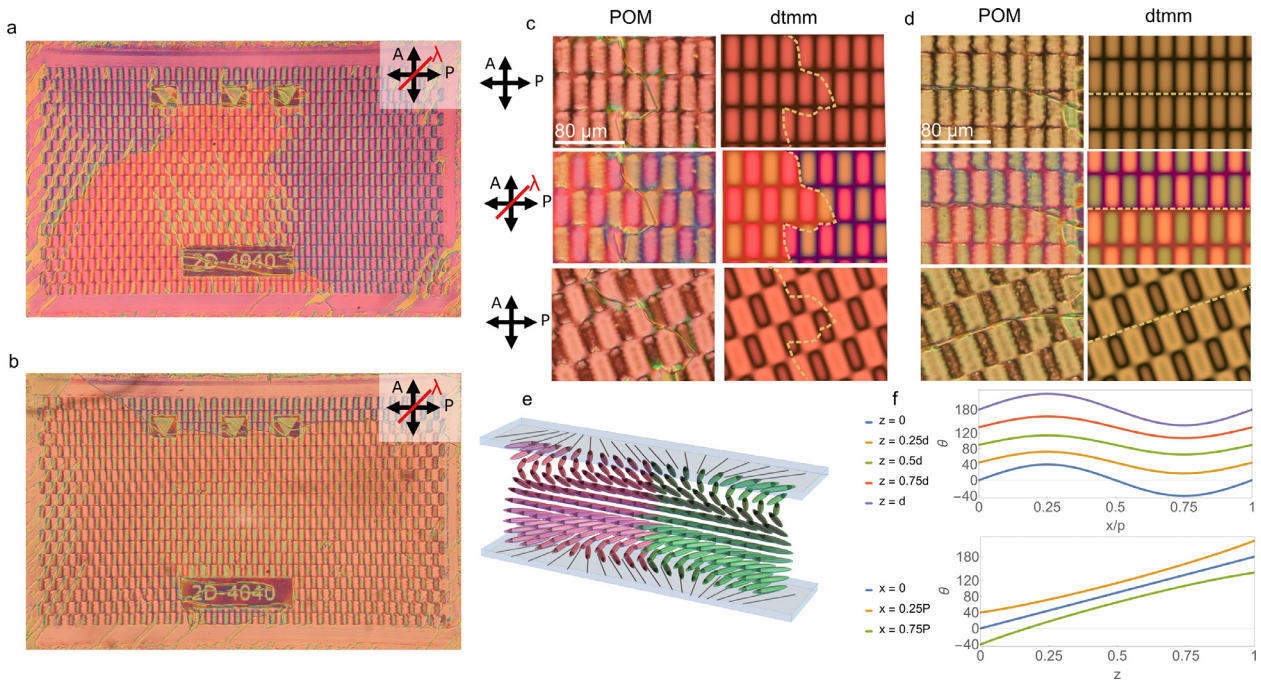

Fig. 3

RM734 in pattern A for cells with thickness 8.1 and 10.1 μm. a&b) Overview of the complete patterned area between crossed polarizers and with the lambda plate for the 8.1 and 10.1 μm cells, respectively. c) Comparison for three geometries of the POM observations and dtmm simulations considering a π-twisted structure across the wall dividing two domains of opposite handedness for the 8.1 μm cell. d) Comparison for three geometries of the POM observations and dtmm simulations considering a π-twisted structure across the wall dividing two domains of opposite handedness for the 10.1 μm cell. In both cases $\xi = 1$ is considered. e) 3D sketch of the director structure used in dtmm simulations including one handedness twist, where colors denote regions with opposite surface splay .f) In-plane ϑ angle along x-direction at different levels through the cell thickness (top) and along the cell thickness at different x positions (bottom) for $\xi = 0.5$ corresponding to the 3D structure depicted in (e) .

arrays, in which adjacent domains exhibit maximum generated SHG signal for incoming pump polarizations at different angles. Results are summarized in Fig. 4 for both thicknesses and, in addition to the pattern with $\vartheta_0 = 40°$ and $P = 2\pi/k$= 40 µm (A40P40), for a pattern in which $\vartheta_0 = 60°$ and $P = 2\pi/k$= 60 µm (A60P60). The analysis of the angle dependence of the intensity throughout the pattern shows that the maximum intensity is obtained at 40 and 120° (where 90° correspond to the vertical direction in the images) for the A40P40 patterns (Fig. 4a-b & d-e), with only a slight difference depending on the cell thickness, while for A60P60 the angles correspond to 20 and 140° (Fig. 4.g & h). Such features are well reproduced in SHG simulations (Fig. 4c, f & i) considering the same structure used in Fig. 3 for POM. A slight asymmetry can also be observed in the intensity profile through the motif. This observation is interesting as, in order to reproduce it in simulations, a certain degree of unsplay is required close to the surface so as the twist profile slightly varies throughout the pattern. Patterns considering a perfect linear twist throughout the motif (i.e. $\xi = 10$) do not reproduce the intensity asymmetries. It is important to note here that simulations for these twisted structures showed little dependence on the value of d_{31}, which was varied in the range from 0 to 0.1 d_{33}.

Inspired by these results, we investigated the effect of sample thickness on the expected SHG signal and angle for the maximum signal for the considered π twisted structure and for a structure with 2π linear twist across the cell. Results for the A40P40 and A60P60 patterns are given in Fig. SI.9. The maximum SHG intensity at each of the complementary areas of the patterns follows a periodic dependence for both π and 2π twisted structures, with the maximum and minimum positions being shifted by half a period between both twists. In the thickness regions in which the signal is near the maximum, little variations are observed in terms of the incoming polarization angles for which the maximum signal is obtained in both adjacent areas. Around the minima however, larger deviations are obtained.

The results confined in Fig. 4. together with the performed simulations show that the combination of twist and surface varying angles is a promising avenue for achieving 2D SHG active arrays from polar nematic systems.

3.3 Pattern B: splay 2D including bend

The larger NLO coefficients of RM734 make it a more attractive candidate than DIO to explore SHG patterns. However, the high operating temperature impedes its direct implementation for future applications. Thus, this second pattern design was tested and compared for two materials, RM734 and FNLC-1571, as the latter exhibits N_F at room temperature. In addition, for both materials the main component of the second-order dielectric susceptibility tensor is d_{33} (Fig. SI.12), with comparable values.

We first investigated the behaviour of FNLC-1571 in 1D splay patterns comparable to those already explored for DIO and RM734 [26]. Equivalently to what was reported in our previous work,

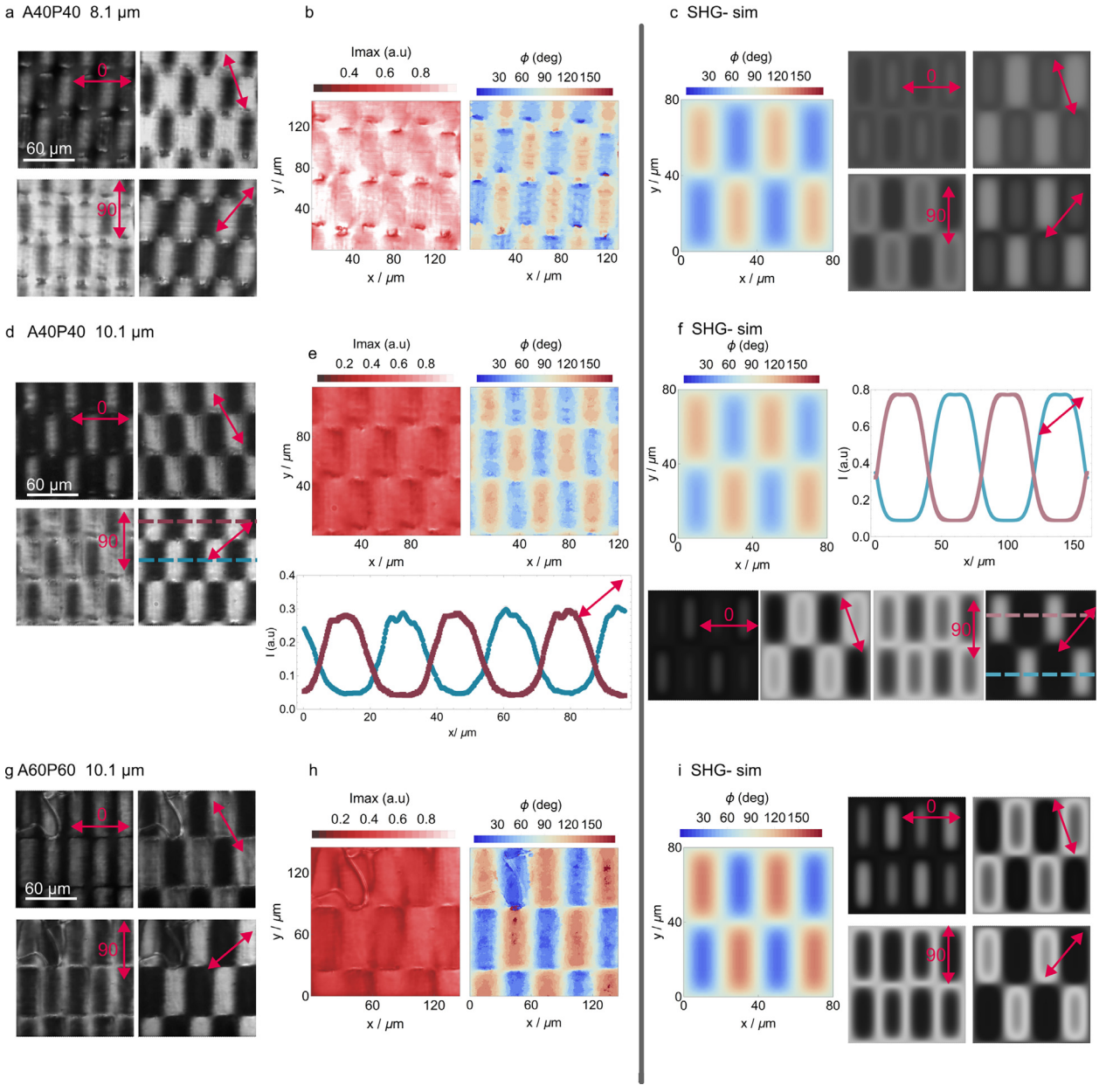

Fig. 4

SHG-M and simulations for RM734 in pattern A in 8.1 and 10.1 μm thick cells. a) SHG-M images for the A40P40 pattern at different incoming pump polarization directions for 8.1 μm cells. b) Analysis of the maximum SHG intensity and corresponding direction of the pump polarization (90° correspond to vertical direction). c) SHG simulated images for the A4040 pattern at different polarizations of the pump beam and corresponding analysis showing the angle at which maximum intensity is obtained. d-f) Equivalent experimental results and simulations as those depicted in a-c, for the same structure in a 10.1 μm cell. Panel (e) includes the intensity profile of the 2D pattern for incoming polarization at 120° through the cuts indicated in d by matching dashed lines. Same analysis is included for simulations in panel f. g-i) Equivalent experimental results and simulations as those depicted in a-c, for the A60P60 pattern in a 10.1 μm cell. Double headed arrows denote the direction of the incoming polarization.

1D motifs result in domains of alternating polarization divided by domain walls placed in those positions in the pattern where splay changes sign. (Fig. SI.10) Investigation of the effect of splay curvature on the patterning success reveals a behaviour closer to that of DIO, indicating that due to the FNLC-1571 characteristics (i.e. flexoelectric coefficients and spontaneous polarization value), the ideal splay curvature is, in this case, larger than in the case of RM734 (Fig. SI.11).

With this basic characterization, we then explored 2D patterns as those depicted in Fig. 5. In this case, sinusoidal modulation was additionally added in y-direction in order to obtain smooth variation in both directions of the splay sign, i.e. $\vartheta_{surf} = A\ \sin[2\pi x/\mathrm{P}]*\sin[2\pi y/\mathrm{P}]$, with $A = 45°$ and P either 40 or 60 μm (Fig. 5.a). Such modulation additionally introduces bend deformation in the structure. Periodicities of 40 and 60 μm with a maximum angle of 45° were explored. Due to the layout

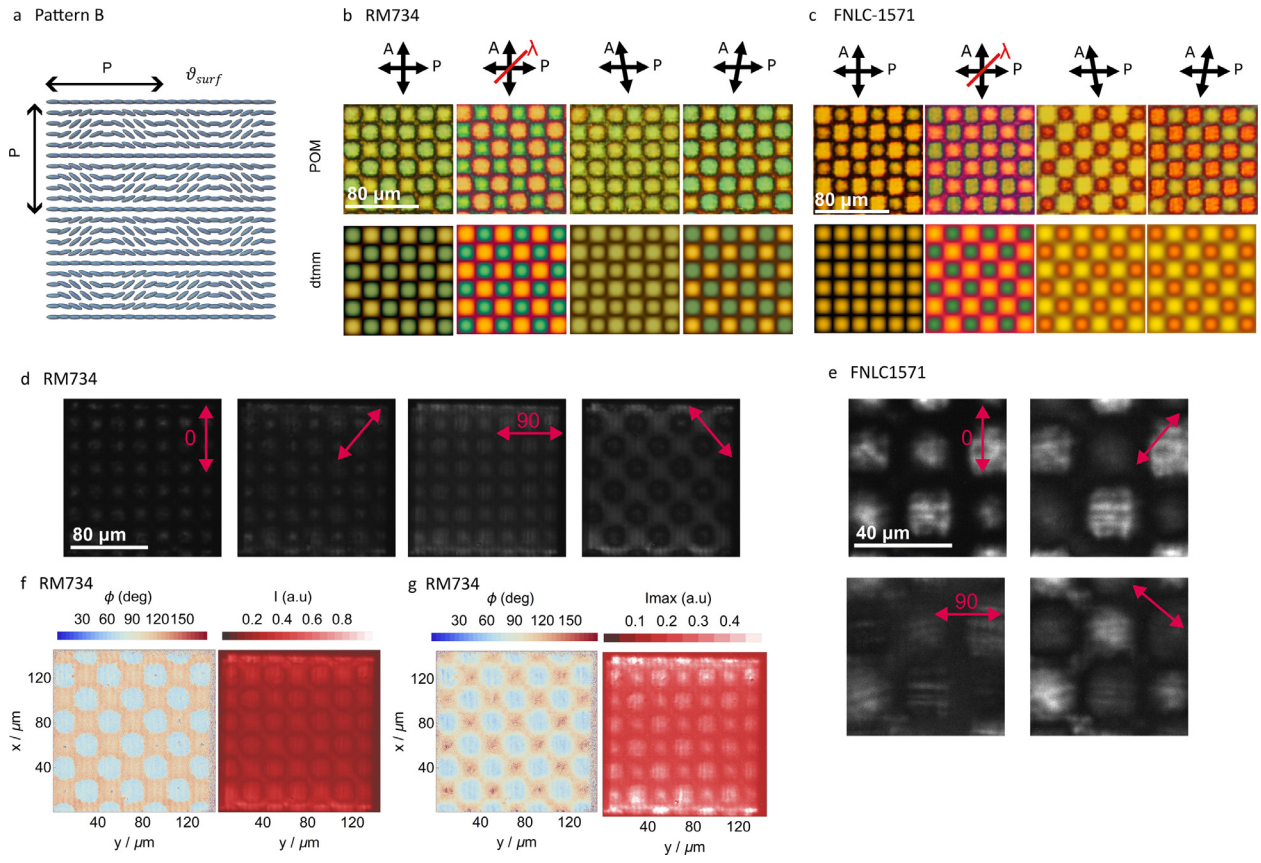

Fig. 5

Pattern B. a) Sketch of the photopatterned design inscribed in both cellś surfaces. b&c) POM images at different conditions (cross polarizers, cross polarizers in combination with a full-wave plate, analyser uncrossed 20° clock- and anti-clockwise) are compared with dtmm transmission spectra simulations for RM734 (b) at 120 °C and FNLC-1571 (c) at room temperature. d) SHG-M images for RM734 recorded for different pump polarizations, indicated by the double headed arrow. e) SHG-M images for FNLC-1571 recorded for different pump polarizations. f) Analysis of the angle of incoming polarization for which maximum SHG signal is obtained (left) and the corresponding maximum intensity. Analysis is done pixel by pixel. g) Equivalent analysis as for (f) but for experiments performed using an analyser along the main direction of the pattern, i.e. horizontal.

of the photopatterned cells, for each material, two equivalent patterns were investigated. Interestingly, two kinds of behaviour are observed. While one of the patterns is practically defect-free, the other shows a scramble of domain walls running along y-direction, undulating according to the pattern's bend (Fig. SI.13). Such opposed behaviour speaks for the instability of the structure for this design, in which details of small thickness gradients, inhomogeneities and surrounding unpatterned areas can tilt the scales towards one or another structure. Here we analyse some details of the defect-free pattern.

In the case of FNLC-1571, the patterns throughout the area mostly show monocolor behaviour under crossed polarizers, with variations only observed close to the edges of the pattern (Fig. SI.14). POM observations under different geometries are well reproduced by dtmm simulations considering again a structure that twists across the cell thickness in order to achieve a uniform director orientation (Fig. 5.c and Fig. SI.14). This "unsplay" is again well reproduced by $\xi = 0.2$ and $\vartheta_{center} = 0°$. The slight colour variations between adjacent areas observed in the case of RM734 between crossed polarizers can be reproduced considering a small deviation in the middle of the cell $\vartheta_{center} = 5°$ (Fig. 5.b) while for such areas in FNLC-1571 ϑ_{center} is found to be closer to 15°. With this in mind, for SHG experiments in FNLC-1571 we will focus on the centre of the motif where uniform behaviour is observed, i.e. $\vartheta_{center} = 0°$.

SHG microscopy images for both materials in pattern B are shown in Fig. 5 (Fig. 5.d for RM734 and Fig. 5.e for FNLC-1571) for different incoming pump polarization directions. Fig. 5.f & g. shows the analysis of the maximum SHG recorded signal throughout the pattern together with the incoming pump polarization direction at which such maximum intensity is recorded for RM734. Although a clearly distinguishable angle dependence can be observed, the intensity contrast between adjacent areas is small. Notably, the analysed area for RM734 shows a sharp change of incoming pump polarization angle for maximum intensity in measurements performed without analyser, while a smooth variation is observed employing an analyser. Such observation speaks for the importance of NLO coefficients other than d_{33} for the design of SHG active arrays. It should be noted here that it was found that SHG simulations for such untwisted structures are drastically sensitive to the combination of input dispersion, cell thickness and NLO

coefficient values in comparison to the twisted structures, and thus can show misleading results in the range of $d_{31}=d_{15}=0$ and $d_{31}=d_{15}=0.1d_{33}$.

It is interesting to note here, that FNLC-1571 was maintained at room temperature (N_F) for a year, after which optical and SHG experiments were repeated for assessing the stability of the structure. Over the course of a year, the monodomain pattern remained stable, without decaying in multiple domains. However, the structure throughout the whole motif relaxed into the structure with the director pointing uniformly at around 12° in the centre of the cell (Fig. SI.15). Consequently, SHG signal profile across the pattern was maintained, with just a slight shift in the angular behaviour with respect to the original state (Fig. SI.15c). Similar stability was found for patterns filled with DIO (pattern A and 1D structures [26]), which were kept at 68 °C for half a year. The higher temperature needed for RM734 prevented such kind of study, but patterns remained unaltered during the experiments spanning over several days, during which the sample was kept at 120 °C. Summarizing for the pattern B in which the motif is based on smooth modulation in both directions, which in addition to splay deformation involves bend, a clear dependence on the pump polarization angle with respect to the pattern is obtained for adjacent areas. However, the inclusion of bend seems to strongly destabilize the structure, in the way that equal patterns can results either in large structured monodomains or in the decay in multiple domains.

4 Conclusions

To conclude, we have demonstrated the pathway towards the fabrication of tailored NLO arrays in the micrometre range, by exploiting patterned photoalignment possibilities. The controlled spatial modulations of SHG on a micrometre scale combined with the possibility of tunability present an advantage of using N_F as photonic structures in comparison to the solid NLO materials. We show that a balance between flexoelectric and electrostatic energy minimization can be used to create a number of structures. However, one should note that material parameters (i.e. spontaneous polarization, ideal splay curvature) combined with design parameters (i.e. cell thickness, periodicity and amplitude of the splay patters) all impact the final achieved structure. In addition, the NLO coefficients together with the dispersion of refractive indices for the target wavelengths also determine the final SHG operational behaviour of the motifs.

For the two investigated patterns based on simple splay structures, we show that in order to minimize electrostatic energy and avoid the creation of strongly charged domain walls, the different materials adapt to unfavourable splay in different ways. Notably, for RM734 large monodomain patterns are obtained with the director at the surfaces following the prescribed alignment and rapidly twisting towards a uniform direction in the middle of the cell. This represents an advantageous scenario when increasing the cell thickness, as such surface structure is shown to procure the decay of the pattern into two 180° twisted domains of opposite handedness, as seen for pattern A. Such twisted structures are shown to be highly profitable from the perspective of achieving 2D SHG active arrays showing strong contrast between adjacent areas for opposite angles (Fig. 4). Considering the importance of the twisted structures for the final SHG patterning, a very promising avenue is to combine such surface boundary conditions to ferroelectric cholesteric nematics with micrometre size pitches, discriminating one handedness by the selection of suitable chiral dopant, which should result in large monodomain patterned areas. It is interesting to note here that for ferroelectric cholesteric nematics phase-matched SHG near the photonic bandgap has been recently reported [20,21]. Additionally, precise control and alignment of N^*_F is not only promising for creating photonic structures but also for the design of N^*_F based lasers with enhanced lasing properties and optimized tunability [36,37].

It should be noted that the design optimization will greatly benefit from a detailed model for ferroelectric nematic materials, allowing to input the material parameters to predict energy minimizing structures. In combination with accurate knowledge of materials parameters and SHG simulations, such a model would greatly expedite the implementation of ferroelectric nematics as key photonic materials.

Declaration of competing interest

The authors declare that they have no known competing financial interests or personal relationships that could have appeared to influence the work reported in this paper.

Data availability

Data will be made available upon reasonable request. Code for diffractive transfer matrix method (dtmm) optical simulations is deposited in Github/Zenodo at "Andrej Petelin. (2020). IJSComplexMatter/dtmm: Version 0.6.1 (V0.6.1)", under accession code https://doi.org/10.5281/zenodo.4266242.

CRediT authorship contribution statement

M. Lovšin: Writing – review & editing, Writing – original draft, Methodology, Investigation, Formal analysis, Data curation. **A. Petelin:** Writing – review & editing, Software, Formal analysis. **B. Berteloot:** Writing – review & editing, Methodology, Data curation. **N. Osterman:** Writing – review & editing, Methodology, Investigation. **S. Aya:** Writing – review & editing, Resources. **M. Huang:** Writing – review & editing, Resources. **I. Drevenšek-Olenik:** Writing – review & editing, Supervision, Funding acquisition. **R.J. Mandle:** Writing – review & editing, Resources. **K. Neyts:** Writing – review & editing, Methodology, Funding acquisition. **A. Mertelj:** Writing – review & editing, Supervision, Methodology, Conceptualization. **N. Sebastian:** Writing – review & editing, Writing – original draft, Visualization, Supervision, Formal analysis, Data curation, Conceptualization.

Acknowledgements

The ferroelectric nematic liquid crystal FNLC-1571 used in this work was supplied by Merck Electronics KGaA. N.S, A.M, I.D-O., M.L, N.O, and A.P acknowledge the support of the Slovenian Research Agency (grant numbers P1–0192, N1–0195, J1–50004 and PR-11214–1). K.N and B.B would like to acknowledge the support of the Research Foundation—Flanders (FWO) through grant number G0C2121N. R.J.M. acknowledges funding from

UKRI via a Future Leaders Fellowship, grant No. MR/W006391/1. S.A. and M.H. acknowledge the National Key Research and Development Program of China (No. 2022YFA1405000) and the Recruitment Program of Guangdong (No. 2016ZT06C322).

Supplementary materials

Supplementary material associated with this article can be found, in the online version, at doi:10.1016/j.giant.2024.100315.

References

[1] S.K. Saha, G.K. Wong, Phase-matched electric-field-induced second-harmonic generation in a nematic liquid crystal, Opt. Commun. 30 (1979) 119–121, doi:10.1016/0030-4018(79)90056-7.

[2] S.K. Saha, G.K. Wong, Investigation of nematic ordering using electric-field-induced second-harmonic generation, Appl. Phys. Lett. 34 (1979) 423–425, doi:10.1063/1.90821.

[3] M.I. Barnik, L.M. Blinov, A.M. Dorozhkin, N.M. Shtykov, Generation of the second optical harmonic induced by an electric field in nematic and smectic liquid crystals, J. Exp. Theo. Phys. 54 (1981) 935–938.

[4] L.M. Blinov, M.I. Barnik, H. Ohoka, M. Ozaki, N.M. Shtykov, K. Yoshino, Surface and flexoelectric polarization in a nematic liquid crystal 5CB, Eur. Phys. J. E 4 (2001) 183–192, doi:10.1007/s101890170127.

[5] H. Nishikawa, K. Shiroshita, H. Higuchi, Y. Okumura, Y. Haseba, S. Yamamoto, K. Sago, H. Kikuchi, A fluid liquid-crystal material with highly polar order, Adv. Mater. 29 (2017) 1702354, doi:10.1002/adma.201702354.

[6] R.J. Mandle, S.J. Cowling, J.W. Goodby, A nematic to nematic transformation exhibited by a rod-like liquid crystal, Phys. Chem. Chem. Phys. 19 (2017) 11429–11435, doi:10.1039/C7CP00456G.

[7] N. Sebastián, L. Cmok, R.J. Mandle, M.R. de la Fuente, I. Drevenšek Olenik, M. Čopič, A. Mertelj, Ferroelectric-ferroelastic phase transition in a nematic liquid crystal, Phys. Rev. Lett. 124 (2020) 037801, doi:10.1103/PhysRevLett.124.037801.

[8] X. Chen, E. Korblova, D. Dong, X. Wei, R. Shao, L. Radzihovsky, M.A. Glaser, J.E. Maclennan, D. Bedrov, D.M. Walba, N.A. Clark, First-principles experimental demonstration of ferroelectricity in a thermotropic nematic liquid crystal: polar domains and striking electro-optics, P. Natl. Acad. Sci. USA (2020) 202002290, doi:10.1073/pnas.2002290117.

[9] N. Sebastián, M. Čopič, A. Mertelj, Ferroelectric nematic liquid-crystalline phases, Phys. Rev. E 106 (2022) 021001, doi:10.1103/PhysRevE.106.021001.

[10] C.L. Folcia, J. Ortega, R. Vidal, T. Sierra, J. Etxebarria, The ferroelectric nematic phase: an optimum liquid crystal candidate for nonlinear optics, Liq. Cryst. 49 (2022) 899–906, doi:10.1080/02678292.2022.2056927.

[11] R. Xia, X. Zhao, J. Li, H. Lei, Y. Song, W. Peng, X. Zhang, S. Aya, M. Huang, Achieving enhanced second-harmonic generation in ferroelectric nematics by doping D–π–A chromophores, J. Mater. Chem. C 11 (2023) 10905–10910, doi:10.1039/D3TC01384G.

[12] J. Li, R. Xia, H. Xu, J. Yang, X. Zhang, J. Kougo, H. Lei, S. Dai, H. Huang, G. Zhang, F. Cen, Y. Jiang, S. Aya, M. Huang, How far can we push the rigid oligomers/polymers toward ferroelectric nematic liquid crystals? J. Am. Chem. Soc. (2021), doi:10.1021/jacs.1c09594.

[13] J. Yang, Y. Zou, W. Tang, J. Li, M. Huang, S. Aya, Spontaneous electric-polarization topology in confined ferroelectric nematics, Nat. Commun. 13 (2022) 7806, doi:10.1038/s41467-022-35443-7.

[14] N. Sebastián, R.J. Mandle, A. Petelin, A. Eremin, A. Mertelj, Electrooptics of mm-scale polar domains in the ferroelectric nematic phase, Liq. Cryst. 48 (2021) 2055–2071, doi:10.1080/02678292.2021.1955417.

[15] V. Sultanov, A. Kavčič, E. Kokkinakis, N. Sebastián, M.V. Chekhova, M. Humar, Tunable entangled photon-pair generation in a liquid crystal, Nature (2024) 1–6, doi:10.1038/s41586-024-07543-5.

[16] H. Nishikawa, F. Araoka, A new class of chiral nematic phase with helical polar order, Adv. Mater. 33 (2021) 2101305, doi:10.1002/adma.202101305.

[17] X. Zhao, J. Zhou, J. Li, J. Kougo, Z. Wan, M. Huang, S. Aya, Spontaneous helielectric nematic liquid crystals: electric analog to helimagnets, Proc. Natl Acad. Sci. 118 (2021), doi:10.1073/pnas.2111101118.

[18] D. Pociecha, R. Walker, E. Cruickshank, J. Szydlowska, P. Rybak, A. Makal, J. Matraszek, J.M. Wolska, J.M.D. Storey, C.T. Imrie, E. Gorecka, Intrinsically chiral ferronematic liquid crystals: an inversion of the helical twist sense at the chiral nematic – Chiral ferronematic phase transition, J. Mol. Liq. 361 (2022) 119532, doi:10.1016/j.molliq.2022.119532.

[19] C. Feng, R. Saha, E. Korblova, D. Walba, S.N. Sprunt, A. Jákli, Electrically tunable reflection color of chiral ferroelectric nematic liquid crystals, Adv. Opt. Mater. 9 (2021) 2101230, doi:10.1002/adom.202101230.

[20] X. Zhao, H. Long, H. Xu, J. Kougo, R. Xia, J. Li, M. Huang, S. Aya, Nontrivial phase matching in helielectric polarization helices: universal phase matching theory, validation, and electric switching, in: Proceedings of the National Academy of Sciences, 119, 2022, doi:10.1073/pnas.2205636119.

[21] X. Zhao, H. Long, J. Li, M. Huang, S. Aya, High-g-factor phase-matched second harmonic generation near photonic bandgap of polar cholesteric liquid crystals, Liq. Cryst. (2024) 1–7 0, doi:10.1080/02678292.2024.2307447.

[22] Y.-T. Hsiao, I. Nys, K. Neyts, Lateral electric field switching in thin ferroelectric nematic liquid crystal cells, Soft. Matter. 19 (2023) 8617–8624, doi:10.1039/D3SM00997A.

[23] J.-S. Yu, J.H. Lee, J.-Y. Lee, J.-H. Kim, Alignment properties of a ferroelectric nematic liquid crystal on the rubbed substrates, Soft. Matter. 19 (2023) 2446–2453, doi:10.1039/D3SM00123G.

[24] X. Chen, E. Korblova, M.A. Glaser, J.E. Maclennan, D.M. Walba, N.A. Clark, Polar in-plane surface orientation of a ferroelectric nematic liquid crystal: polar monodomains and twisted state electro-optics, Proc. Natl Acad. Sci. 118 (2021), doi:10.1073/pnas.2104092118.

[25] P. Kumari, B. Basnet, M.O. Lavrentovich, O.D. Lavrentovich, Chiral ground states of ferroelectric liquid crystals, Science 383 (2024) 1364–1368, doi:10.1126/science.adl0834.

[26] N. Sebastián, M. Lovšin, B. Berteloot, N. Osterman, A. Petelin, R.J. Mandle, S. Aya, M. Huang, I. Drevenšek-Olenik, K. Neyts, A. Mertelj, Polarization patterning in ferroelectric nematic liquids via flexoelectric coupling, Nat. Commun. 14 (2023) 3029, doi:10.1038/s41467-023-38749-2.

[27] R.J. Mandle, S.J. Cowling, J.W. Goodby, Rational design of rod-like liquid crystals exhibiting two nematic phases, Chem. Eur. J. 23 (2017) 14554–14562, doi:10.1002/chem.201702742.

[28] J. Li, H. Nishikawa, J. Kougo, J. Zhou, S. Dai, W. Tang, X. Zhao, Y. Hisai, M. Huang, S. Aya, Development of ferroelectric nematic fluids with giant-ε dielectricity and nonlinear optical properties, Sci. Adv. 7 (2021) eabf5047, doi:10.1126/sciadv.abf5047.

[29] X. Chen, Z. Zhu, M.J. Magrini, E. Korblova, C.S. Park, M.A. Glaser, J.E. Maclennan, D.M. Walba, N.A. Clark, Ideal mixing of paraelectric and ferroelectric nematic phases in liquid crystals of distinct molecular species, Liq. Cryst. 49 (2022) 1531–1544, doi:10.1080/02678292.2022.2058101.

[30] R.J. Mandle, N. Sebastián, J. Martinez-Perdiguero, A. Mertelj, On the molecular origins of the ferroelectric splay nematic phase, Nat. Commun. 12 (2021) 4962, doi:10.1038/s41467-021-25231-0.

[31] I. Nys, B. Berteloot, J. Beeckman, K. Neyts, Nematic liquid crystal disclination lines driven by a photoaligned defect grid, Adv. Opt. Mater. 10 (2022) 2101626, doi:10.1002/adom.202101626.

[32] A. Petelin, IJSComplexMatter/dtmm: version 0.6.1, (2020). https://doi.org/10.5281/zenodo.4266242.

[33] J. Ortega, C.L. Folcia, J. Etxebarria, Second harmonic generation in anisotropic stratified media: a generalization of the Berreman method and its application to photonic materials, Opt. Express 31 (2023) 36966–36980 OE, doi:10.1364/OE.497447.

[34] A. Petelin, andrej5elin/dtmm2: V0.1.0, (2024). https://doi.org/10.5281/zenodo.11608823.

[35] A.G. Khachaturyan, Development of helical cholesteric structure in a nematic liquid crystal due to the dipole-dipole interaction, J. Phys. Chem. Solids 36 (1975) 1055–1061, doi:10.1016/0022-3697(75)90044-X.

[36] C.L. Folcia, J. Ortega, T. Sierra, A. Martínez-Bueno, J. Etxebarria, Chiral ferroelectric nematic liquid crystals as materials for versatile laser devices, (2024). 10.48550/arXiv.2402.12420.

[37] J. Ortega, C.L. Folcia, J. Etxebarria, T. Sierra, Ferroelectric chiral nematic liquid crystals: new photonic materials with multiple bandgaps controllable by low electric fields, Liq. Cryst. 49 (2022) 2128–2136, doi:10.1080/02678292.2022.2104949.